Journal of Solar Energy Research (JSER)

Journal homepage: www.jser.ut.ac.ir

Photovoltaic System RL-based MPPT and Active Disturbance Control Using Dynamic Surface and RL Induction Motor Control for Photovoltaic Water Pumping System

Boubacar Kirgni Hamza[a], Noma Talibi Soumaila[a,*], Attoumane Kosso Moustapha[b], Boureima Seibou[b]

[a]*Laboratory of Energy, Electronics, Electrotechnics, Automatics and Industrial Computing, Abdou Moumouni University (UAM), Niamey, Niger*
[b]*Laboratory for Research in Engineering and Environmental Technical Sciences (STIE), Mines, Industry and Geology School, Niamey, Niger.*

ARTICLE INFO

Article Type:

Research Article

Received:2025.12.12
Accepted in revised form:2026.02.14

Keywords:
Reinforcement learning;
Photovoltaic water pumping systems;
Active disturbance rejection control;
Dynamic surface control;
Proportional-integral-derivative

A B S T R A C T

Photovoltaic water pumping systems (PVWPSs) are increasingly deployed in remote and off-grid regions where grid extension is technically infeasible or economically prohibitive. However, their performance is significantly affected by fluctuating solar irradiance, temperature variations, and the nonlinear dynamics of the electric motor and mechanical load. To address these challenges, this paper proposes an integrated control framework combining reinforcement learning (RL)–based strategy for the PV optimal operating point tracking and ADRC scheme enhanced by dynamic surface control (DSC) and RL-based induction motor (IM) speed regulation. The RL-based MPPT estimates the MPP, while the ADRC–DSC structure with RL compensation ensures smooth speed tracking while effectively rejecting load torque disturbances. The proposed control strategy is evaluated through comprehensive simulations and benchmarked against conventional P&O/IM-based PID and sliding mode control (SMC) approaches. Quantitative results demonstrate that the proposed method achieves up to 97.7% and 89% reduction in power oscillations compared to P&O/PID and SMC, respectively. Moreover, the normalized speed mean square error (NSMSE) is reduced by 13.9% and 2.1% compared with P&O/PID and SMC, respectively. Additional improvements in torque estimation accuracy, current quality, flux ripple mitigation, and water pumping efficiency confirm the robustness and effectiveness of the proposed control framework.

*Corresponding Author Email: nomasoumaila@gmail.com

Cite this article: Hamza, B. K., Soumaïla, N. T., Moustapha, A. K. and Seibou, B. (2026). RL-based MPPT and Active Disturbance Control using Dynamic surface and RL Induction Motor control for Photovoltaic Water Pumping System. Journal of Solar Energy Research, 11(1), 2903-2922. doi: 10.22059/jser.2026.408032.1686

DOI: 10.22059/jser.2026.408032.1686

1. Introduction

Energy plays a fundamental role in supporting modern society and economic development. Since the industrial revolution, global energy demand has increased rapidly, resulting in accelerated depletion of fossil fuel resources. This trend threatens the long-term sustainability of human civilization. At the same time, greenhouse gas emissions from conventional energy generation have continued to rise, intensifying climate change and environmental degradation. Addressing these challenges requires a global transition toward low-carbon energy systems that ensure secure, clean, and affordable energy access. In this context, renewable energy sources have emerged as viable and sustainable alternatives. Among them, solar energy has attracted particular attention due to its abundance, wide availability, and minimal environmental impact, making it a promising solution for sustainable energy development [1].

Photovoltaic water pumping systems (PVWPSs) have gained increasing importance, especially in remote and isolated regions where grid extension is technically difficult or economically unfeasible. In such areas, PV-based pumping solutions represent an effective tool for promoting sustainable development. Among the available solar energy technologies, PV systems are the most broadly implemented solution for the direct generation of electrical power from sunlight. In PVWPSs, electricity generated by PV arrays has been used to drive water pumps for domestic supply, irrigation, and livestock watering [2] and [3]. Several studies reported that, when properly designed, PVWPSs offered a cost-effective and energy-efficient alternative to conventional grid-connected or diesel generator–driven pumping systems, particularly in rural applications [4], [5] and [6]. Despite these advantages, PVWPSs continue to face several technical challenges. These challenges include the nonlinear current–voltage characteristics of PV arrays, the inherently low conversion efficiency of PV modules, and the presence of a single operating point corresponding to maximum power extraction that varied with irradiance and temperature [7], [8], [9] and [10]. Therefore, maintaining operation at the photovoltaic array's optimal power condition is a critical factor in achieving high system efficiency.

To address these challenges and ensure reliable performance, it is essential to implement effective control strategies for PVWPSs [11]. Indeed, optimal control not only enhances system efficiency but also ensures stable and robust operation under varying environmental conditions. Over the years, researchers have proposed a wide range of control techniques for PVWPSs, including maximum power point tracking (MPPT) methods, frequency stabilization, voltage regulation and load matching. Among these, MPPT plays a particularly critical role, as this mechanism ensures that the PV array operates close to its optimal power point even in the presence of irradiance and temperature variations. MPPT algorithms are generally grouped into two categories: conventional approaches, most effective under uniform irradiance, and advanced approaches that rely on stochastic optimization or artificial intelligence. While conventional methods are simple and widely adopted, they often struggle to maintain accuracy in conditions of partial shading or rapid variations in solar radiation [12]. Commonly used conventional algorithms include fractional short-circuit current (Isc), Incremental Conductance (InCond), Hill Climbing (HC), Perturb and Observe (P&O), fractional open-circuit voltage (Voc), ripple correlation control and load current/voltage maximization. Within this class of techniques, the P&O and InCond algorithms are widely adopted because they offer a good balance between implementation simplicity and tracking accuracy [12]. In the P&O technique, the operating voltage of the PV array is incrementally modified, and the resulting power variation is analyzed to guide the adjustment process. Unlike P&O, the InCond method determines voltage regulation by analyzing the relative behavior of instantaneous conductance (I/V) and incremental conductance ($\Delta I/\Delta V$), thereby enhancing the accuracy of maximum power point tracking.

Despite their widespread adoption, the aforementioned conventional methods often suffer from persistent deviations around the optimal power operating condition and reduced responsiveness under rapidly varying operating conditions. Similarly, traditional proportional–integral (PI) controllers with fixed gains lack adaptability, making them less effective in compensating for parameter variations and environmental uncertainties. These limitations typically result in slower response times and reduced tracking accuracy. To overcome such challenges, researchers have increasingly turned to advanced intelligent control strategies. For instance, in Stitou et al. (2019) [13], an output-feedback control approach was developed for sensorless PV systems with integrated MPPT, while Stitou et al. (2022) [14] proposed an adaptive output-feedback scheme for uncertain PV systems. Both studies employed backstepping-based techniques, which, although effective, may encounter practical difficulties due to

the well-known "explosion of complexity" inherent to conventional backstepping methods. Further, Djeriou et al. (2018) [15] investigated the Golden Section Search (GSS) method to enhance the overall efficiency of standalone PV water pumping systems (SPWPS). This approach demonstrated robustness, immunity to perturbations, and improved system efficiency, resulting in higher water output and faster transient response. The algorithm directly determines the reference voltage and current values. Although effective, this method involves significant computational overhead and requires considerable time during implementation. Chen et al. (2025) [16] presented an irradiance-sensorless MPPT controller for photovoltaic systems based on PSO-assisted integral backstepping and immersion–invariance control, achieving zero overshoot, fast convergence, and high efficiency. The proposed control technique was validated through simulations and microcontroller-in-the-loop experiments; however, further validation on full hardware platforms and under severe partial shading and long-term operating conditions remains necessary. Abena Malobe et al. (2023) [17] proposed an MPPT controller that employs a Neuro-Fuzzy approach for PV arrays affected by partial shading. The designed controller improves tracking accuracy and power extraction, though the study focuses on specific shading scenarios, limiting generalizability. Imani and Delavari (2017) [18] optimized a PD-type fuzzy controller using Particle Swarm Optimization, enhancing tracking speed and accuracy under varying conditions. Yet, the developed control technique may face challenges related to computational complexity and performance under highly dynamic or partial shading environments. Xiao et al. (2026) [19] developed an MPPT strategy combining Long Short-Term Memory neural networks with the Improved Hunger Games Search Optimization Algorithm. The designed controller improves prediction and convergence speed, though its complexity and reliance on training data may limit real-time application and generalization. Ali et al. (2025) [20] designed a robust Backstepping Super-Twisting MPPT controller for dynamic shading conditions that reduces power fluctuations and improves response time. Yet, the increased algorithmic complexity could hinder the developed controller's real-time implementation and scalability. Dunna et al. (2024) [21] introduced a Super-Twisting MPPT control using a higher-order sliding mode observer for grid-connected PV/battery systems, enhancing robustness and reducing chattering, but the complexity may raise computational demands, limiting applicability in large-scale or cost-sensitive installations.

Other contributions have explored artificial intelligence (AI)-driven approaches. In Priyadarshiet al. (n.d.) [22], with the integration of an adaptive neuro-fuzzy inference system (ANFIS) with a modern Luo converter and the Flower Pollination Algorithm (FPA), the system produced precise PV outputs and eliminated steady-state oscillations around the maximum power point under fluctuating solar irradiance. Similarly, Akkaya et al. (2007) [23] introduced a multilayer perceptron neural network optimized with a genetic algorithm (GA) for MPPT applications, employing the Levenberg–Marquardt algorithm for training, whereas Elkholy et al. (2016) [24] applied an ANN-based controller to a three-phase induction motor pump (IMP) system, allowing the PV array to deliver maximum power under dynamic environmental conditions while limiting losses in the motor. Moreover, El-Khatib et al. (2017) [25] proposed a Simplified Universal Intelligent PID (SUI-PID) approach, demonstrating superior rise time and faster transient response compared to standard fuzzy logic controllers. Although such intelligent methods demonstrate superior precision and faster dynamic response compared to classical techniques, they often involve high computational complexity and intricate design requirements [12].

Since the motor is responsible for driving the pump, it has a significant impact on the performance of a PVWPS. Several studies have emphasized the significance of motor selection and control in solar pumping applications, as an efficient motor reduces the required number of PV modules for a given power demand, thereby lowering the system's capital cost [26]. Based on the application, both DC and AC motors have been widely employed in PVWPSs. In the early stages of solar pumping development, DC motors were often preferred due to their ability to interface directly with PV panels, which generate direct current. However, AC induction motors (IMs) are now more common because of their robustness and suitability for large-scale pumping applications, though their nonlinear dynamics make control challenging [27]. The scalar control approach is frequently used for its simplicity and cost-effectiveness, yet it exhibits poor torque performance at low operating frequencies [28]. To overcome this limitation, indirect field-oriented control (IFOC) has been introduced, offering precise speed regulation and consistent torque delivery across a wide speed range [29] and [30]. Nevertheless, IFOC performance is dependent on precise motor parameter identification, which can be difficult to maintain in real-world operating conditions. Direct Torque Control (DTC) is increasingly adopted as a promising

alternative, providing direct regulation of flux and torque without extensive reliance on machine parameters. Its simplified structure eliminates the need for inner current loops, while delivering faster dynamic response, higher efficiency, and stronger robustness under variable conditions [31], [32], [33] and [34]. For speed control, proportional–integral (PI) controllers remain the most commonly applied solution due to their simplicity and ease of implementation. Yet, they exhibit drawbacks such as overshoot, oscillations, and sluggish transient response, particularly under load variations or parameter uncertainties [35]. These shortcomings highlight the necessity of advanced control strategies to ensure high efficiency and reliability in PV-driven motor systems. Within PVWPS applications, deploying an optimal speed controller not only enhances system dynamics but also enables earlier operation, increases water yield, and extends daily runtime. As a result, solar energy utilization is maximized, leading to improved productivity and greater reliability under fluctuating environmental conditions.

Sequential decision-making problems are common in both natural and engineered systems. For example, an infant learning to walk performs a series of trial-and-error actions, receives feedback from the environment, and gradually improves its gait. This process is formally described by the Markov Decision Process (MDP) framework, which provides a structured mathematical approach for representing decision-making in uncertain environments. An MDP is characterized by four elements: the transition probabilities T(s,a,s'), the set of actions A, the set of states S and the reward function R(s,a,s'). Reinforcement Learning (RL) builds upon this framework, enabling an agent to learn a decision-making policy $\pi(a|s)$ by directly interacting with the environment. The agent selects an action, observes the new state and numerical reward, and then improves its policy over time to maximize cumulative reward. Among various RL algorithms, Q-learning is widely used due to its simplicity and effectiveness: it learns the optimal state–action values by iteratively updating a Q-table using temporal-difference (TD) learning. The trade-off between exploration and exploitation is commonly handled through an ε-greedy policy, which balances random exploration of actions with the exploitation of learned knowledge.

In the context of PV energy systems, MPPT represents a sequential decision-making problem well suited to RL. The PV system operates in a nonlinear environment influenced by irradiance and temperature variations, making the location of the maximum power point (MPP) dynamic and uncertain. Traditional MPPT methods such as P&O or IncCond rely on deterministic rules and often suffer from oscillations or slow converge when environmental conditions change quickly. By contrast, RL-based MPPT treats the controller as an agent and the PV array as its environment: the state is defined by operating conditions (such as changes in power), the action corresponds to adjusting the control input (voltage or duty cycle perturbation), and the reward reflects the improvement in harvested power. The agent interacts with the PV system in discrete steps, learns from the observed feedback, and adapts its control policy online, thereby overcoming the limitations of static rule-based approaches.

Although existing studies, such as Chou et al. (2019) [36], have demonstrated the feasibility of applying Q-learning to MPPT, many of these approaches rely on large state–action discretization and directly update the duty cycle, leading to high memory demand and potential instability in hardware implementation. In this work, we propose a simplified RL-Q MPPT framework that introduces several innovations. This study makes the following contributions:

- A novel reinforcement learning–based MPPT strategy is proposed in which the state space is reduced to only two states (power increasing and power decreasing). This drastic reduction significantly lowers computational complexity and memory requirements compared to existing RL-based MPPT approaches.

- Unlike conventional RL-MPPT methods that directly perturb the duty cycle, the proposed approach adjusts the reference voltage associated with the estimated MPP. The duty cycle is computed indirectly from the converter's input–output relationship, resulting in smoother control action, improved stability, and enhanced hardware safety.

- An integrated control architecture is developed that jointly addresses energy extraction and motor drive performance. The proposed framework combines the simplified RL-based MPPT with an active disturbance rejection controller (ADRC) based dynamic surface control (DSC) and RL technique for the electric motor to ensure fast and robust speed control, while mitigating the adverse effects of load disturbances. By jointly optimizing energy extraction and motor speed regulation, the proposed approach significantly enhances system

efficiency, water yield, and operational reliability of PVWPSs.

The remainder of the paper is structured as follows. In Section 2, the modeling of the PVWPS is presented. Section 3 outlines the proposed control methodology. Section 4 reports simulation outcomes and comparative evaluations. Finally, Section 5 summarizes the main conclusions.

2. Design of the PVWPS

In this section the PVWPS is established. The PVWPS is designed with key components including solar panels, a DC-DC boost converter, a Voltage Source Inverter (VSI) and an IM that drives a centrifugal pump as shown in figure 1. To maximize energy extraction from the solar panels, MPPT is employed, adjusting the DC-DC boost converter's duty cycle in real-time. Additionally, DTC is applied to the IM via the VSI, enabling precise and efficient management of the motor's performance. In the following, the dynamics governing each component of the PVWPS will be presented. For components where the dynamics are not explicitly detailed, the corresponding models and equations can be found in the relevant references [31], [32] and [33].

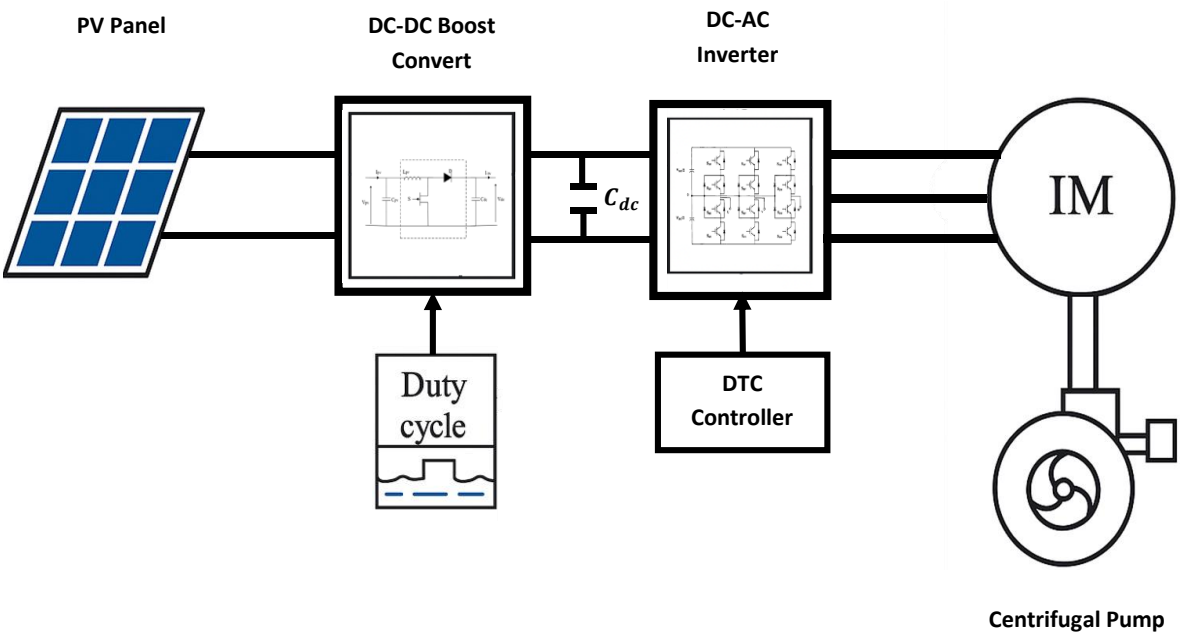

Figure 1. The PVWPS considered in this study

2.1. PV panel

The quantity of PV panels is determined in proportion with respect to the nominal power rating of the IM, which in this study is specified as 1.5 kW. To account for the inherent losses within the PVWPS, the generated power must exceed the nominal power rating of the IM. The PV system selection is guided by the relevant equation as follows

$$P_{mpp} = N_p \times I_{mpp} \times N_s \times V_{mpp} \quad (1)$$

Table 1. The characteristics of the PV model

Parameters	PV Array model	PV Single model
Short circuit current (I_{cc}) [A]	8.48	8.48
Open circuit voltage (V_{oc}) [V]	36.96	295.68
Maximum power (P_{mpp}) [W]	235	1880
Maximum current (I_{mpp}) [A]	7.99	7.99
Maximum voltage (V_{mpp}) [V]	235.36	29.42

In this study, the numerical simulations employ eight PV panels configured in series to fulfill the required energy demand effectively. The model of the PV array is implemented within the Matlab/Simulink platform adopting the T5-SER-235P module. The selected single PV module and the configured PV array model detailed characteristics are provided in table 1. Figure 2 illustrates the simulated I–V and P–V characteristics of the PV module in Simulink, obtained under Standard Test Conditions (STC) of 25 °C temperature and 1000 W/m² irradiance.

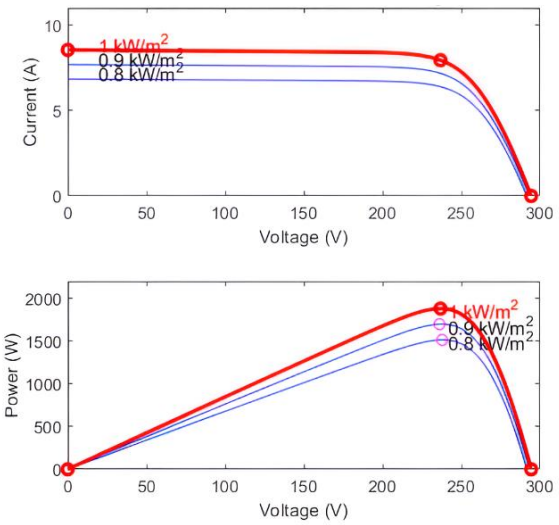

Figure 2. the current–voltage (I–V) and power–voltage (P–V) curves generated from the PV module model

2.2. PV Solar Module

Figure 3 presents the widely utilized equivalent model of a solar module with a single diode configuration, showing its electrical representation and characteristics. This model is commonly employed in photovoltaic system analyses and simulations due to its simplicity and effectiveness in representing module behavior under varying conditions.

The PV array output current, formed by the combination of series and parallel PV panels, can be computed using the following formula [35]

$$I_{pv} = N_p I_{ph} - N_p I_0 \left(\exp\left(\frac{1}{V_t}\left(\frac{V_{pv}}{N_s} + \frac{RI_{pv}}{N_p}\right) - 1\right) - \frac{N_p}{R_{sh}}\left(\frac{V_{pv}}{N_s} + \frac{RI_{pv}}{N_p}\right)\right) \quad (2)$$

with $V_t = \frac{\alpha k T}{q}$.

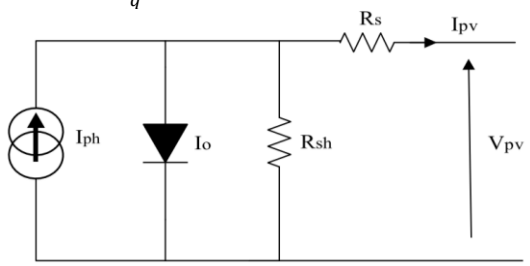

Figure 3. Equivalent model of a solar module

2.3. DC-DC Boost converter

A DC–DC converter operating in boost mode serves as an intermediate regulator, linking the photovoltaic array to the inverter. In this system, the converter's main purpose is to elevate the PV array's input voltage V_{pv} to a higher DC voltage V_{dc} for downstream components. This voltage conversion is determined by the converter's duty cycle α, which is controlled using MPPT techniques. Figure 4 depicts the DC-DC boost converter equivalent circuit.

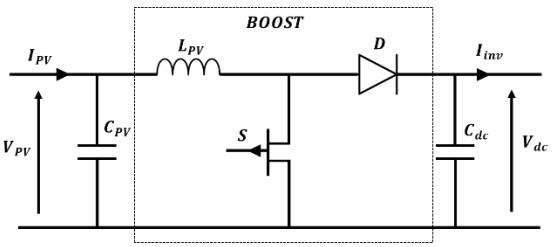

Figure 4. Boost converter.

To guarantee continuous conduction mode (CCM) operation, the boost converter parameters—namely the duty cycle α, the input inductance L_{pv}, and the DC-link capacitance C_{dc}—are carefully selected. The duty cycle α is computed using the relationship given below

$$\alpha = 1 - \frac{V_{mppv}}{V_{dc}} \quad (3)$$

The value of the boost converter inductor is obtained based on the relationship given below

$$L_{pv} = \frac{\alpha V_{mppv}}{\Delta I f_s} \quad (4)$$

The inverter input DC-bus voltage V_{dc} is selected according to the rated characteristics of the induction motor. The calculation typically follows the relationship

$$V_{dc} = \frac{2\sqrt{2}}{\sqrt{3}} V_{LL} \quad (5)$$

with V_{LL} stands for IM RMS line voltage.

The DC-link capacitor voltage is designed to provide sufficient energy buffering during operating disturbances, including variations in environmental conditions and load demand, and is calculated using the expression below

$$C_{dc} = \frac{6\alpha V_{LL} I_L t}{\sqrt{3}(V_{dc}^{*2} - V_{dc}^2)} \quad (6)$$

where I_L is the line current of IM, V_{dc} and V_{dc}^* are respectively the measured and reference values of the DC bus voltage and t is the time duration that the DC link voltage needs to be modified. The boost converter computation parameters are given in table 2.

Table 2. Boost converter parameter values

Parameters	Values
V_{dc}^* [V]	400
C_{dc} $[\mu F]$	1172
A	0.41
L [mH]	3

2.4. Induction Motor (IM)

Various types of motors are employed in solar-powered water pumping systems, each with unique characteristics. For instance, synchronous reluctance motors [37], induction motors (IM) [38], [39] and permanent magnet synchronous motors [40] have all been explored for driving water pumps. Among these, induction motors are commonly favored in PVWP applications due to their robust design, widespread industrial use, cost-effectiveness, and affordability. These qualities make them a reliable choice compared to other commercially available motor types [41].

The IM dynamics in the $(\alpha - \beta)$ reference frame can be expressed through mathematical equations that account for its electrical and mechanical behavior. These equations typically involve variables such as stator and rotor currents, voltages, flux linkages, and electromagnetic torque, described in the two-phase $(\alpha - \beta)$ coordinate system. The IM parameters are provided in table 3.

Voltages of rotor and stator in the (α-β) reference frame [31]

$$\begin{cases} 0 = R_r I_{r\alpha} + \frac{d\phi_{r\alpha}}{dt} + \omega_m \phi_{r\beta} \\ 0 = R_r I_{r\beta} + \frac{d\phi_{r\beta}}{dt} + \omega_m \phi_{r\alpha} \\ V_{s\alpha} = R_s I_{s\alpha} + \frac{d\phi_{s\alpha}}{dt} \\ V_{s\beta} = R_s I_{s\beta} + \frac{d\phi_{s\beta}}{dt} \end{cases} \quad (7)$$

Table 3. IM parameters

Parameters	Values	Parameters	Values
Nominal power [KW]	1.5	R_r [Ω]	4
Nominal current [A]	6.4/3.7	L_s [H]	0.47
Number of pole pair	P=2	L_r [H]	0.47
Frequency [Hz]	50	M [H]	0.44
Rated speed [rpm]	1410	J [Kg/m]	0.04
Factor of power	0.83	F [N.msec/rad]	0.002
Voltage [V]	220/380	R_s [Ω]	8

Fluxes of rotor and stator in the $(\alpha - \beta)$ reference frame

$$\begin{cases} \phi_{r\alpha} = L_r I_{r\alpha} + M I_{s\alpha} \\ \phi_{r\beta} = L_r I_{r\beta} + M I_{s\beta} \\ \phi_{s\alpha} = L_s I_{s\alpha} + M I_{r\alpha} \\ \phi_{s\beta} = L_s I_{s\beta} + M I_{r\beta} \end{cases} \quad (8)$$

where L_r, L_s, R_r and R_s respectively represent the rotor and stator inductors and resistors, M is the mutual inductor, and $I_{r\alpha}$, $I_{r\beta}$, $I_{s\alpha}$ and $I_{s\beta}$, are the rotor and stator current in the $(\alpha - \beta)$ frame, respectively.

The electromagnetic torque T_e produced by the IM governs its rotational dynamics [33]

$$\begin{cases} T_e = \frac{3}{2} p\left(\phi_{s\alpha} I_{s\beta} - \phi_{s\beta} I_{s\alpha}\right) \\ T_e - T_l = J\dot{\omega} + b\omega \end{cases} \quad (9)$$

The mathematical model of the three-level neutral-point-clamped (NPC) inverter is expressed in the following matrix form as

$$\begin{bmatrix} v_a \\ v_b \\ v_c \end{bmatrix} = \frac{1}{3} V_{dc} \begin{bmatrix} 2 & -1 & -1 \\ -1 & 2 & -1 \\ -1 & -1 & 2 \end{bmatrix} \begin{bmatrix} T_{11}T_{12} - T_{12}T_{14} \\ T_{21}T_{22} - T_{23}T_{24} \\ T_{31}T_{32} - T_{33}T_{34} \end{bmatrix} \quad (10)$$

Figure 5 below presents the schematic representation of the three-level NPC inverter.

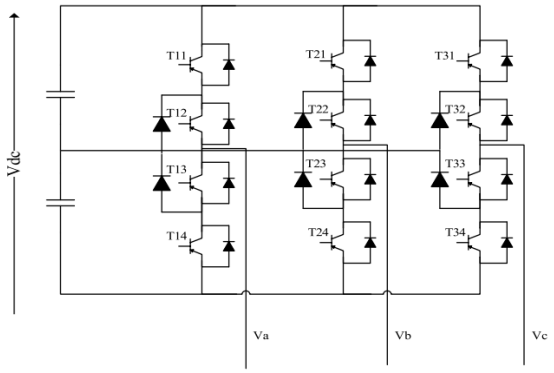

Figure 5. Three-level NPC inverter structure

2.5. Centrifugal Pump

The torque demand of the centrifugal pump is modeled as being proportional to the square of the induction motor rotor speed

$$T_{pump} = K_{pump}\omega^2 \tag{11}$$

3. Proposed System Control Framework

This section outlines the development of two distinct control strategies tailored to enhance the PVWPS performance. The first control law is designed to optimize the operation of the photovoltaic (PV) subsystem, with a focus on maximizing energy extraction and improving overall power conversion efficiency. The second control strategy is dedicated to regulating the induction motor (IM) that drives the centrifugal pump, aiming to maintain stable and efficient operation under varying load and environmental conditions.

3.1. MPPT based Reinforcement Learning design

In this section, an advanced control strategy is developed to realize an intelligent MPPT controller capable of reliably extracting the maximum power from the PV array under fast-changing irradiance and temperature conditions. The proposed MPPT strategy is formulated as a RL problem in which the PV system acts as the environment and the controller as the learning agent. At each sampling instant k, the agent observes the PV panel voltage V_k, current I_k and bus voltage V_{out} from which the instantaneous power $P_k = V_k I_k$ is computed. A reward signal is defined as the incremental power change $r_k = P_k - P_{k-1}$, which provides immediate feedback on whether the previous action improved the operating condition. The system state is discretized into two categories: $s_k = 1$ if power increases ($r_k \geq 0$) and $s_k = 2$ if power decreases ($r_k < 0$), enabling a compact Q-table representation. Based on the current state, an action a_k is chosen either randomly with probability ε to ensure exploration, or greedily from the Q-table to exploit prior knowledge. The action corresponds to perturbing the reference voltage by $\pm\Delta V$, yielding a candidate reference $V_{k+1}^{ref,*}$ which is then clamped to safe bounds $\left[V_{min}^{ref}, V_{max}^{ref}\right]$. The associated duty cycle is calculated as $\alpha_{k+1} = 1 - \frac{V_{k+1}^{ref}}{V_{out}}$ and further constrained within $[\alpha_{min}, \alpha_{max}]$ before being applied to the converter. Learning occurs through a temporal-difference (TD) update, where the previous state-action pair Q-value is adjusted as

$$Q(s_{k-1}, a_{k-1}) \leftarrow Q(s_{k-1}, a_{k-1}) + \vartheta\big(r_k + \gamma \max_{a'} Q(s_k, a') - Q(s_{k-1}, a_{k-1})\big) \tag{12}$$

Table 4 summarizes the pseudo-code used to implement the proposed MPPT strategy, while Figure 6 illustrates the corresponding flowchart.

Table 4. Pseudo-code of Q-learning Vmpp-reference MPPT

Inputs (at step k)

Measured PV voltage V_k, PV current I_k, DC-bus voltage V_{out}

Persistent Variables

Q-table $Q \in \mathbb{R}^{2\times 2}$, previous state s_{k-1}, previous action a_{k-1}, previous power P_{k-1}, previous reference voltage V_k^{ref}

Hyperparameters

Learning rate $\vartheta > 0$, discount factor $\gamma \in [0,1)$, exploration rate $\varepsilon \in [0,1]$, voltage step $\Delta V > 0$, reference bounds $V_{\min}, V_{\max}$, duty limits $\alpha_{\min}, \alpha_{\max}$

Procedure (at step $k \rightarrow k+1$)

1. **Power Measurement and Reward Computation**

   $P_k \leftarrow V_k I_k$

   $r_k \leftarrow P_k - P_{k-1}$

2. **State Determination**

$$s_k = \begin{cases} 1, & r_k \geq 0 \text{(power increase)} \\ 2, & r_k < 0 \text{(power decrease)} \end{cases}$$

3. **Action Selection (ε-greedy)**

- With probability ε: select a_k randomly
- Otherwise:

$$a_k \leftarrow \arg\max_a Q(s_k, a)$$

4. **MPP Reference Voltage Update**

$$V_{k+1}^{\text{ref},*} = \begin{cases} V_k^{\text{ref}} + \Delta V, & a_k = 1 \\ V_k^{\text{ref}} - \Delta V, & a_k = 2 \end{cases}$$

$$V_{k+1}^{\text{ref}} \leftarrow \text{sat}(V_{k+1}^{\text{ref},*}, V_{\min}, V_{\max})$$

5. **Q-Table Update (Temporal-Difference Learning)**

$$\delta_k \leftarrow r_k + \gamma \max_{a'} Q(s_k, a') - Q(s_{k-1}, a_{k-1})$$

$$Q(s_{k-1}, a_{k-1}) \leftarrow Q(s_{k-1}, a_{k-1}) + \vartheta \delta_k$$

6. **Duty Cycle Computation**

$$\alpha_{k+1} \leftarrow 1 - \frac{V_{k+1}^{\text{ref}}}{V_{\text{out}}}$$

7. **Duty Cycle Scheduling and Saturation**

$$\alpha_{\min}, \alpha_{\max} = \begin{cases} [\alpha_{\min}, \alpha_{\max}], & k < k_{\text{sch}} \\ [\alpha_{\min}, \alpha_{\max}], & k \geq k_{\text{sch}} \end{cases}$$

$$\alpha_{k+1} \leftarrow \text{sat}(\alpha_{k+1}, \alpha_{\min}, \alpha_{\max})$$

8. **Variable Update**

$$P_{k-1} \leftarrow P_k, s_{k-1} \leftarrow s_k, a_{k-1} \leftarrow a_k, V_k^{\text{ref}} \leftarrow V_{k+1}^{\text{ref}}$$

9. **Output:** Duty cycle α_{k+1}

Remark 1. The primary benefit of scheduling duty-cycle bounds in the Q-learning–based MPPT algorithm lies in enhancing stability and ensuring reliable convergence during startup and the early stages of learning. By restricting abrupt variations in the duty cycle at system initialization, the controller avoids sudden voltage and current transients that could otherwise stress both the PV module and the power converter. This precaution is particularly critical at the beginning, when the Q-learning agent has limited knowledge of the system dynamics. Without such bounds, large duty-cycle adjustments could induce significant power fluctuations, leading to a noisy and less informative reward signal. Gradually constraining duty variations allows the algorithm to learn in a more controlled manner, thereby improving the smoothness and stability of the learning process.

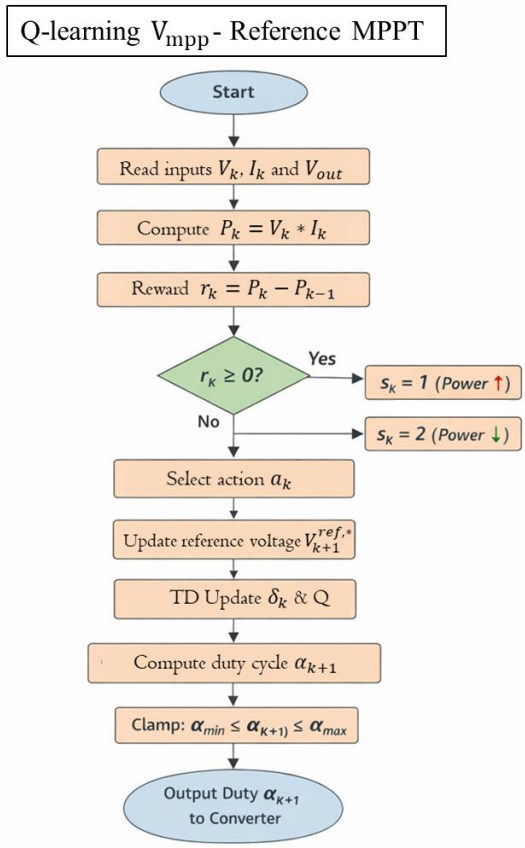

Figure 6. Proposed MPPT based Reinforcement Learning flowchart

3.2. Active disturbance rejection control based dynamic surface and RL IM control

3.2.1 Problem Formulation and Control Objective

The control strategy adopted in this work is Direct Torque Control (DTC), which regulates the electromagnetic torque T_e by directly selecting appropriate stator voltage vectors. By ensuring fast torque response, DTC allows the motor speed to closely track its reference.

To enhance robustness against load disturbances and parameter uncertainties, an Active Disturbance Rejection Control (ADRC) scheme combined with Dynamic Surface Control (DSC) and Reinforcement Learning (RL) is proposed. In this framework, the IM speed is regulated through DTC, while disturbances are estimated online using an extended observer augmented with RL.

Considering the mechanical dynamics of the IM, the rotor speed ω is governed by

$$J\dot{\omega} = b\omega + T_e - T_l \tag{13}$$

where T_l is the load torque T_e is the mechanical torque, ω is the rotor speed, J and b are the IM design parameters.

By virtue of Euler's discretization technique, the above presented continuous mathematical model of IM rotor speed can be transformed into the following discrete-time form

$$\omega_{t+1} = \left(1 - \frac{bT_s}{J}\right)\omega_t + \frac{T_s}{J}u_t - \frac{T_s}{J}d_t \tag{14}$$

where $u_t = T_e$, $d_t = T_l$ is viewed as disturbance to the system and T_s is sampling period.

3.2.2. RL-Enhanced Extended State Observer (ESO)

Within the ADRC framework [42], the disturbance d_t is incorporated as an additional system state. A second-order Extended State Observer (ESO) is constructed to estimate both the rotor speed and the lumped disturbance. Unlike conventional ESOs, the proposed observer integrates an RL agent to improve disturbance estimation accuracy. The observer dynamics are defined as

$$\begin{cases} \widehat{\omega}_{t+1} = \left(1 - \frac{bT_s}{J}\right)\widehat{\omega}_t + \frac{T_s}{J}u_t - \frac{T_s}{J}\hat{d}_t + l(\omega_t - \widehat{\omega}_t) \\ \hat{d}_{t+1} = \nu \end{cases} \tag{15}$$

where $\widehat{\omega}_t$ and $\hat{d}_t$ are the estimate of ω_t and d_t, respectively and l is the observer gain which is obtained by means of bandwidth-parameterization strategy [43].

3.2.3. Actor Neural Network for Disturbance Estimation

In the proposed scheme, the disturbance estimate ν is generated by an actor neural network. The actor learns an optimal policy $\pi(\cdot|\, s)$ that maps the system state to an action a, representing the disturbance estimate.

Let ν denote the output of the actor neural network, which provides the total disturbance estimate, with $a \sim \pi(\cdot|\, s)$. The ideal policy model can be expressed as $\pi = \theta^* \rho_a(s) + \varepsilon_a^*$, while its practical approximation is represented by $\hat{\pi} = \theta \rho_a(s)$, where a is the corresponding action and s denotes the RL state. The loss function corresponding to the policy π is constructed by employing the Kullback–Leibler (KL) divergence, which quantifies the discrepancy between the ideal and the approximated policies, and is given by

$$L_\theta(t) = \frac{1}{N}\sum_{i=1}^{N}\left(\mu log\big(\pi(a|s)\big) - \hat{J}(s,a)\right) \tag{16}$$

where, μ represents the regularization coefficient. To avoid excessive parameter variation, the actor update law is constrained as

$$\theta_{(i)} = \begin{cases} -\rho_a \frac{\partial L_\theta(t)}{\partial \theta_{(i)}}, & 0 \le \frac{\partial L_\theta(t)}{\partial \theta_{(i)}} \le \sigma_a \\ -\rho_a \sigma_a, & \frac{\partial L_\theta(t)}{\partial \theta_{(i)}} > \sigma_a \end{cases} \tag{17}$$

where ρ_a denotes the actor neural NN learning rate, which governs the step size of parameter updates during training.

This online learning mechanism enables the ESO to adapt to changing operating conditions without relying on offline datasets.

3.2.4. Critic Neural Network and Cost Evaluation

The critic network assesses the control policy's long-term performance using the discounted cost function

$$J_c = \sum_{k=0}^{\infty}\beta^k R(t+k) + H(\pi) \tag{18}$$

where $H(\pi)$ is the policy entropy, β denotes the discount factor. The instantaneous reward is defined as

$$R(k) = -\left(Q_{\omega_t} e_t^2 + R_{\omega_t} u_t^2\right) \tag{19}$$

where $e_t = \omega_t - \omega_{t,ref}$ is the tracking error, $\omega_{t,ref}$ is the reference speed, Q_{ω_t} and R_{ω_t} are positive definite weighting matrices. Define the actual cost-to-go function as $J_c(s,a,t) = w^{*T}\delta_c(s,a) + \varepsilon_c^*$ and its approximation as $\hat{J}_c = w^{*T}\delta_c(s,a)$. Since the true $J_c(s,a,t)$ is generally unavailable, the weight update loss function is formulated using a temporal-difference approximation as follows

$$L_w(t) = \frac{1}{2}\left(\varphi(t) + \beta\hat{J}_c(s,a,t+1) - \hat{J}_c(s,a,t)\right)^2 \tag{20}$$

Subsequently, the critic NN update rule is given by

$$\dot{w}_{(i)} = \rho_c \frac{\partial L_w(t)}{\partial w_{(i)}} \tag{21}$$

with ρ_c denoting the critic NN learning rate. To ensure stability and prevent network excessive divergence, the parameter updates are constrained such that $0 \le \frac{\partial L_w(t)}{\partial w_{(i)}} \le \sigma_c$. Under this condition, the parameter update law is expressed as

$$w_{(i)} = \begin{cases} -\rho_c \frac{\partial L_w(t)}{\partial w_{(i)}}, & 0 \le \frac{\partial L_w(t)}{\partial w_{(i)}} \le \sigma_c \\ -\rho_c \sigma_c, & \frac{\partial L_w(t)}{\partial w_{(i)}} > \sigma_c \end{cases} \tag{22}$$

3.2.5. Controller design and stability analysis

To continue with the design of the IM control law, the following Lemma is introduced

Lemma [44]. Considering a given nonlinear system whose states are defined as $\eta_k = \left[\eta_{1,k}, \eta_{2,k}, \dots, \eta_{n,k}\right]^T \epsilon \mathbb{R}^n$ and a Lyapunov functional candidate V_{η_k}. Then, the entire states η_k of the closed-loop is exponentially mean-square (EMS) stable and satisfies

$$\mathbb{E}\{\|\eta_k\|^2\} \le \frac{v_2}{v_1}\|\eta_0\|^2(1-\omega)^k + \frac{\theta}{v_1\omega} \tag{23}$$

with $\eta_0 \epsilon \mathbb{R}^n$ the provided initial condition, if there exist real scalars $v_1 > 0$, $v_2 > 0$, $\theta \ge 0$ and $0 < \omega < 1$ such that

$$v_1\|\eta_k\|^2 \le V_{\eta_k} \le v_2\|\eta_k\|^2 \tag{24}$$

and

$$\mathbb{E}\{V_{\eta_{k+1}|\eta_k} - V_{\eta_k}\} \le \omega V_{\eta_k} + \theta \tag{25}$$

Moreover, the following assumption is made to facilitate the design of IM speed controller in the subsequent section.

Assumption: for $\forall\, t$, the first-order and the second-order differences of the IM speed reference are assumed to be bounded, that is $|\omega_t - a_1 \sum_{i=0}^{t-1} \omega_i| \le b_1$ and $\left|\omega_{t+1,ref} - a_2\omega_{t,ref} - a_3 \sum_{i=0}^{t-1} \omega_i\right| \le b_2$, hold, where $a_{i(i=1,2,3)} > 0$ and $b_{1,2} > 0$ are unknown constants denoting the matching upper bounds.

Hence, a dynamic surface, structured as a proportional-integral is designed as follows

$$S_t = \lambda_1 e_t + \lambda_2 \sum_{i=0}^{t-1} e_i \tag{26}$$

where λ_1 and λ_2 are positive constants.

To ensure rotor speed error convergence, the desired torque can be calculated by

$$u_t = -k\hat{S}_t + k_1\left(\omega_{t,ref} - \widehat{\omega}_t\right) + k_2 \sum_{i=0}^{t-1}\left(\omega_{i,ref} - \widehat{\omega}_i\right) + \frac{1}{\lambda_1}\hat{d}_t \tag{27}$$

Based on Lyapunov's stability theory, the candidate function used for stability assessment is defined by the following expression

$$V_t = S_t^2 \tag{28}$$

Accordingly, the Lyapunov function difference is determined

$$V_{t+1} - V_t = S_{t+1}^2 - S_t^2 = (S_{t+1} - S_t)(S_{t+1} + S_t) \tag{29}$$

Combing equation (14) and (26), the following expression can be derived

$$S_{t+1} = -\frac{\lambda_1 kT_s}{J} S + \frac{\lambda_1 kT_s}{J}\tilde{S} + \left[\left(\lambda_1 + \lambda_2 - \frac{\lambda_1 bT_s}{J} - \frac{\lambda_1 k_1 T_s}{J}\right)\omega_t - \left(\frac{\lambda_1 k_2 T_s}{J} - \lambda_2\right)\sum_{i=0}^{t-1}\omega_i\right] - \left[\lambda_1\omega_{t+1,ref} - \left(\frac{\lambda_1 k_1 T_s}{J} - \lambda_2\right)\omega_{t,ref} - \left(\frac{\lambda_1 k_2 T_s}{J} - \lambda_2\right)\sum_{i=0}^{t-1}\omega_i\right] - \frac{T_s}{J}\tilde{d}_t + \frac{\lambda_1 kT_s}{J}\widetilde{\omega}_t + \frac{\lambda_1 k_2 T_s}{J}\sum_{i=0}^{t-1}\widetilde{\omega}_i \tag{30}$$

Next, it can be readily derived from equation (30) that the following must be hold to satisfy the above assumption

$$\begin{cases} \lambda_1 + \lambda_2 - \frac{\lambda_1 bT_s}{J} - \frac{\lambda_1 k_1 T_s}{J} > 0 \\ \frac{\lambda_1 k_2 T_s}{J} - \lambda_2 > 0 \\ \frac{\lambda_1 k_1 T_s}{J} - \lambda_2 > 0 \end{cases} \tag{31}$$

Accordingly, equation (30) is rewritten as follows

$$S_{t+1} = -\frac{\lambda_1 kT_s}{J} S_t + \Upsilon \tag{32}$$

where $\Upsilon = \left[\left(\lambda_1 + \lambda_2 - \frac{\lambda_1 bT_s}{J} - \frac{\lambda_1 k_1 T_s}{J}\right)\omega_t - \left(\frac{\lambda_1 k_2 T_s}{J} - \lambda_2\right)\sum_{i=0}^{t-1}\omega_i\right] - \left[\lambda_1\omega_{t+1,ref} - \left(\frac{\lambda_1 k_1 T_s}{J} - \lambda_2\right)\omega_{t,ref} - \left(\frac{\lambda_1 k_2 T_s}{J} - \lambda_2\right)\sum_{i=0}^{t-1}\omega_i\right] + \frac{\lambda_1 kT_s}{J}\tilde{S} -$

$\frac{T_s}{J}\tilde{d}_t + \frac{\lambda_1 k T_s}{J}\tilde{\omega}_t + \frac{\lambda_1 k_2 T_s}{J}\sum_{i=0}^{t-1}\tilde{\omega}_i, \quad \tilde{\omega}_t = \omega_t - \hat{\omega}_t,$ $\tilde{S}_t = S_t - \hat{S}_t$ and $\tilde{d}_t = d_t - \hat{d}_t$.

Substituting equation (32) into equation (29) results in

$$V_{t+1} - V_t = (S_{t+1} - S_t)(S_{t+1} + S_t) = \left(-\frac{\lambda_1 k T_s}{J}S_t + \Upsilon - S_t\right)\left(-\frac{\lambda_1 k T_s}{J}S_t + \Upsilon + S_t\right) = \left(-\left(1 + \frac{\lambda_1 k T_s}{J}\right)S_t + \Upsilon\right)\left(\left(1 - \frac{\lambda_1 k T_s}{J}\right)S_t + \Upsilon\right) = -\left(1 - \left(\frac{\lambda_1 k T_s}{J}\right)^2\right)S_t^2 - 2\frac{\lambda_1 k T_s}{J}S_t\Upsilon + \Upsilon^2 \leq -\left(1 - 2\left(\frac{\lambda_1 k T_s}{J}\right)^2\right)S_t^2 + 2\Upsilon^2 \quad (33)$$

In order to ensure that the variation of V_t is negative, i.e.,

$$V_{t+1} - V_t < 0 \quad (34)$$

The controller gain k should satisfy the following condition

$$k < \frac{J}{\lambda_1 T_s \sqrt{2}} \quad (35)$$

Therefore, for any values of the controller gain k that meet condition stated in (35), the inequality $0 < 1 - 2\left(\frac{\lambda_1 k T_s}{J}\right)^2 < 1$ holds. Further, it is always possible to find some arbitrarily scalars $v_1 > 0$ and $v_2 > 0$ such that

$$v_1\|S_t\|^2 \leq V_t \leq v_2\|S_t\|^2 \quad (36)$$

Accordingly, one has

$$V_{t+1} - V_t \leq -\varpi V_t + 2\Upsilon^2 \quad (37)$$

where $\varpi = 1 - 2\left(\frac{\lambda_1 k T_s}{J}\right)^2$.

Referring to the Lemma, the system S_t is EMS-bounded and satisfies

$$\mathbb{E}\{\|S_t\|^2\} \leq \frac{v_2}{v_1}\|S_0\|^2(1-\varpi)^t + \frac{2\Upsilon^2}{\varpi v_1} \quad (38)$$

where S_0 stands for the initial condition.

It follows from (38) that $\tilde{\omega}_t$ is also EMS-bounded. Thus, inequality (37) can be expressed in an alternative form as

$$V_{t+1} \leq (1-\varpi)V_t + 2\Upsilon^2 \quad (39)$$

where its solution can be stated as

$$V_t \leq (1-\varpi)^t V_t(0) + \sum_{i=0}^{t-1} 2\Upsilon^2(1-\varpi)^{t-1-i} \quad (40)$$

and its upper limit is defined as follow

$$\lim_{t\to+\infty} V_t \leq \frac{2\Upsilon^2}{\varpi} \quad (41)$$

The above inequality (41) can further be reformulated in the following

$$\lim_{t\to+\infty} S_t \leq \sqrt{\frac{2\Upsilon^2}{\varpi}} \quad (42)$$

From the preceding analysis, it can be inferred that, the system states S_t will eventually reside in a residual set δ_{S_t} within a finite time step $N_{\delta_{S_t}}$, with the origin as its center, in a uniform manner.

$$\delta_{S_t} = \left\{S_t \,/\, S_t \leq \sqrt{\frac{2\Upsilon^2}{\varpi}}\right\} \quad (43)$$

It is important to highlight that, the state S_t will stay confined within the region δ_{S_t} and will not move outside of it for any subsequent time steps, i.e., for $t > N_{\delta_{S_t}}$, when the state enters this region.

4. Numerical simulation and discussion

Numerical simulations are carried out in this section to evaluate the effectiveness of the proposed control approach. To demonstrate both the effectiveness and robustness of the developed approach, it is compared against a fixed duty cycle bound RL-based MPPT and a PID controller-based speed controller. The overall simulation scheme is presented in Figure 7. The parameter used to carry the simulation are $\vartheta = 0.01$; $\gamma = 0.9$; $\varepsilon = 0.1$, $\Delta V = 0.01$; $Q = 10$; $R = 0.001$; $l = 18000$; $k = 13$; $k_1 = 400$; $k_2 = 400$; $\lambda_1 = 4$; $\lambda_2 = 3$; and $T_s = 0.0001s$. The irradiation as well as the temperature profiles are depicted in Figure 8 respectively.

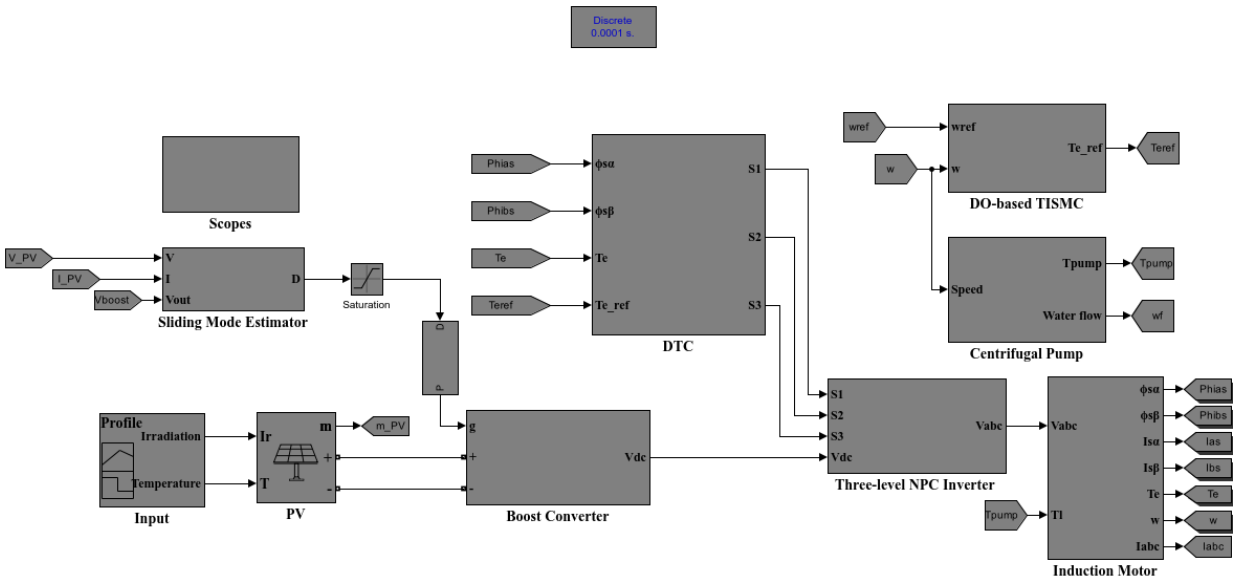

Figure 7. Simulation model

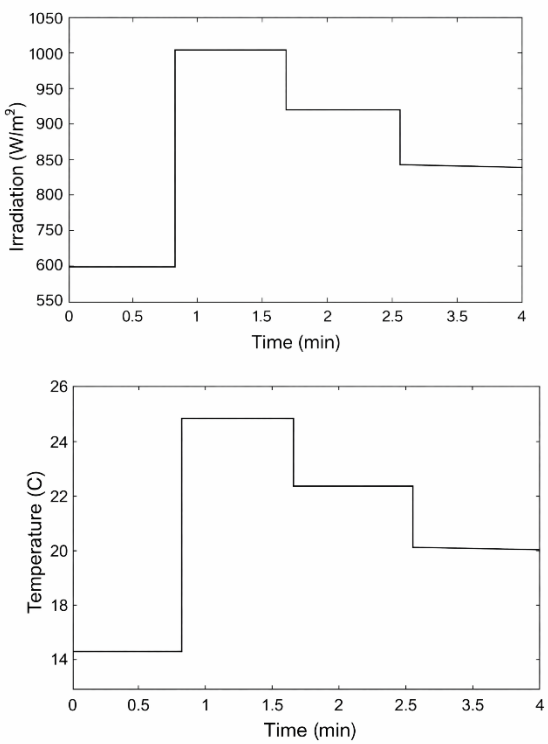

Figure 8. Irradiation and Temperature profiles

The simulation results are depicted in figures 9-15. Specifically, figure 9 depicts the photovoltaic power response, clearly demonstrating the enhanced effectiveness of the proposed RL-based control strategy compared to the fixed-duty-cycle RL-based MPPT. The proposed method exhibits enhanced robustness and significantly reduced oscillations, highlighting its effectiveness. In addition, its maximum power point tracking performance exceeds that of the fixed-duty-cycle RL-based MPPT, as shown in Figure 9.a. Actually, by scheduling the duty cycle bound the system performance is optimized, even during the startup. By using scheduled duty cycle bounds, the PVWPS operates more efficiently while reducing energy waste and provide more water supply.

Figure 10 illustrates the evolution of rotor speed under both control strategies. The results show that the proposed control method achieves faster and more accurate convergence of the rotor speed to its reference compared with the conventional PID controller. In addition, the proposed control method responds more rapidly and tracks the reference signal in less time than the PID controller. This enhanced performance can be attributed not only to the use of the estimate rotor speed but also to the continuous compensation of load torque load using the RL throughout the simulation, enabled by the integrated disturbance estimator. The latter plays a key role in ensuring the convergence rotor speed to its reference value, thereby significantly improving the system's overall precision and efficiency.

Figure 11 presents the electromagnetic torque response for both control strategies. Simulation results indicate that the proposed control strategy substantially minimizes torque ripple relative to the conventional PID controller. Additionally, it ensures accurate tracking of the pump torque, effectively addressing the deviations observed with the PID strategy. This improvement contributes to enhanced system reliability and operational efficiency, while

also minimizing energy losses, mechanical stress, and potential instability in PVWPS.

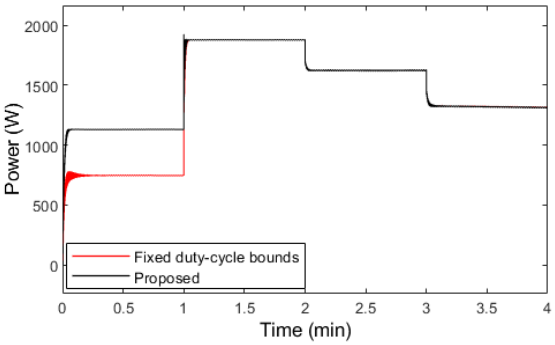

Figure 9. PV power

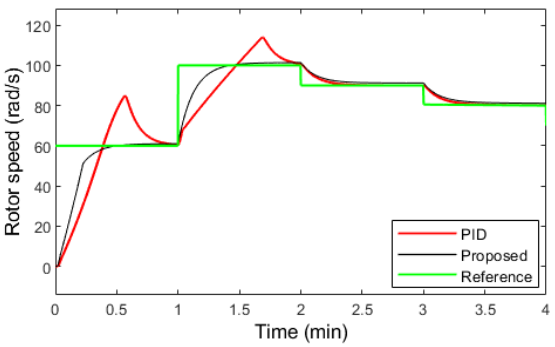

Figure 10. Rotor speed response

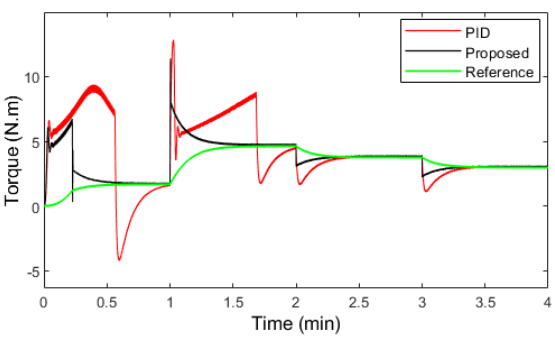

Figure 11. Electromagnetic torque response

Figure 12 illustrates the motor flux responses. The result demonstrates that the proposed control scheme effectively minimizes flux ripple, outperforming the conventional PID controller, highlighting its superior performance and improved smoothness in dynamic operation.

Figure 13 present the evolution of water flow rates. It is evident that the proposed approach leads to a noticeable increase in the volume of pumped water relative to the PID method. This enhancement becomes even more pronounced with increasing rotor speed during variations in solar irradiation, thereby confirming the robustness and adaptability of the proposed control strategy under time-varying conditions.

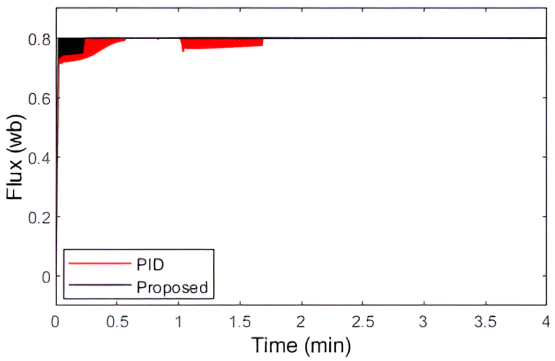

Figure 12. IM flux response

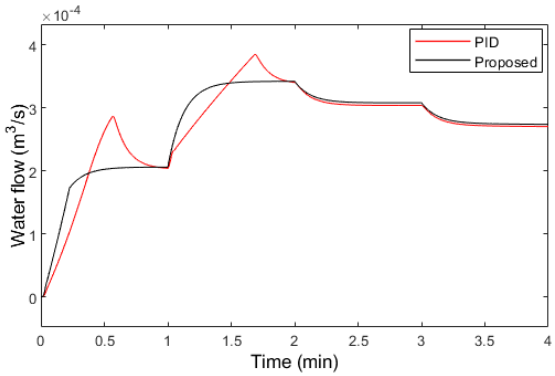

Figure 13. Pumped water response

Figures 14 and 15 show the stator current waveforms. The proposed control technique produces an almost ideal sinusoidal waveform, in contrast to the distorted waveforms observed with the PID. This result underscores the effectiveness of the developed DTC approach in improving current quality, reducing harmonic distortion, and improving the operational effectiveness and energy efficiency of the PVWPS.

To validate the proposed control strategy, a performance comparison is carried out against the conventional P&O-based MPPT method. Furthermore, a quantitative evaluation is performed based on standard performance metrics, namely power oscillations and the normalized induction motor speed mean square error (NSMSE). As illustrated in Figure 16, the proposed approach exhibits a significantly improved dynamic response relative to the P&O strategy.

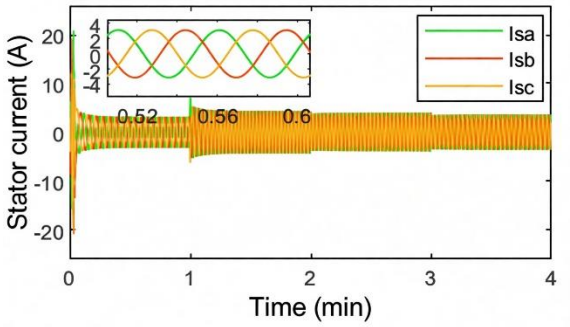

Figures 14. Stator current response under the proposed control approach

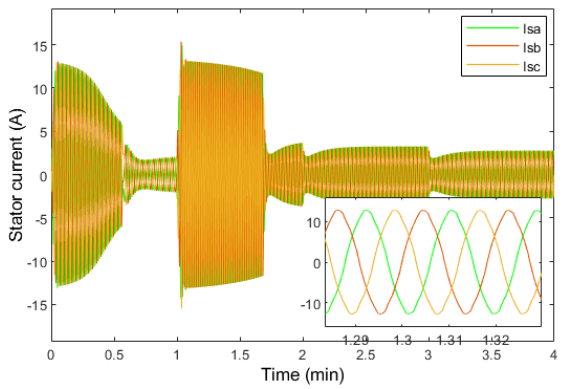

Figures 15. Stator current response under the PID control approach

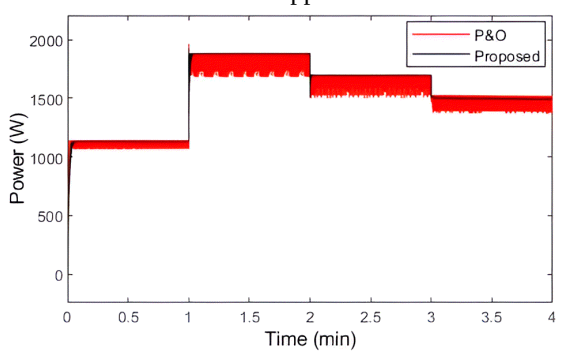

Figure 16. PV output power under the proposed control strategy in comparison with the P&O

In particular, it achieves a substantial reduction in steady-state fluctuations near the MPP, as clearly evidenced in Figure 16 and quantitatively confirmed by the results reported in Table 5. This improvement highlights the superior tracking accuracy and stability of the proposed method under steady operating conditions.

To further assess the robustness of the developed strategy, its performance is evaluated against a sliding mode control (SMC) approach under abrupt disturbances conditions. The corresponding simulation results are presented in Figures 17–23. These results consistently demonstrate that the proposed control scheme outperforms the SMC strategy across multiple performance indices.

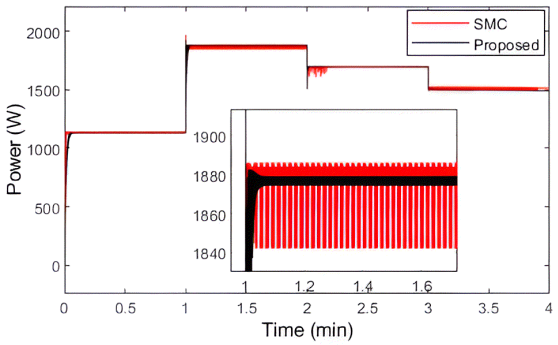

Figure 17. PV output under the proposed control strategy in comparison with the SMC

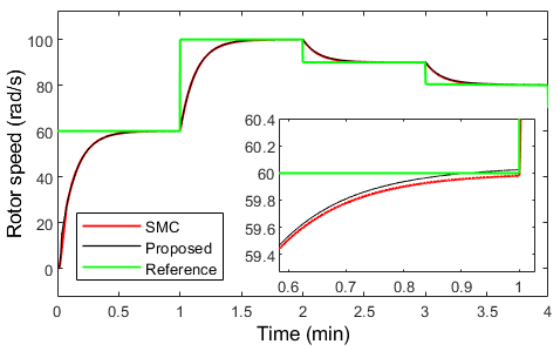

Figure 18. Rotor speed response under the proposed control strategy compared with the SMC

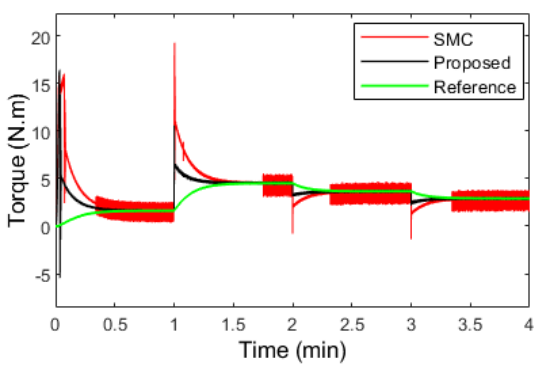

Figure 19. Electromagnetic torque response under the proposed control strategy compared with the SMC

Specifically, Figure 17 shows that the proposed MPPT technique has markedly reduced oscillations compared to the SMC method, indicating enhanced robustness against environment condition variations. Figures 18 and 19 illustrate the responses of rotor

speed and electromagnetic torque, respectively. The results indicate that the proposed control strategy ensures a faster transient response while effectively suppressing torque oscillations, in contrast to the pronounced chattering effects associated with the SMC approach. This behavior is particularly advantageous for reducing mechanical stress and improving the operational lifespan of the pumping system.

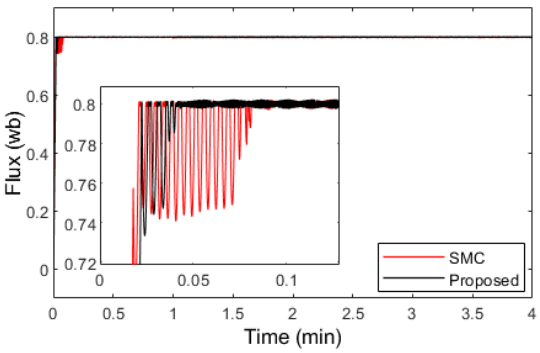

Figure 20. IM flux response under the proposed control strategy compared with the SMC

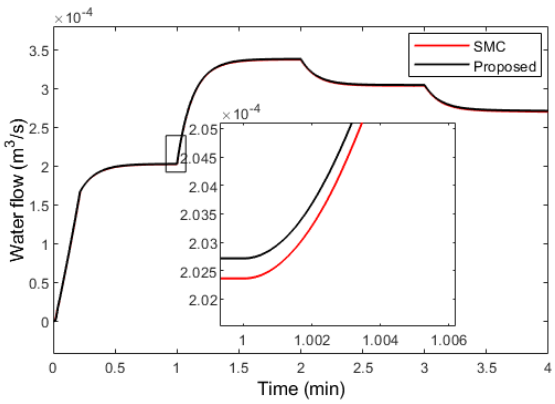

Figure 21. Pumped water response under the proposed control strategy compared with the SMC

The stator flux responses are illustrated in Figure 20. The proposed control method significantly reduces flux ripple relative to the SMC strategy, thereby ensuring smoother electromagnetic operation and improved dynamic performance of the induction motor. This reduction in flux oscillations directly contributes to enhanced efficiency and lower losses.

Figure 21 presents the evolution of the water flow rate. The results indicate that the developed control technique leads to a noticeable increase in the pumped water volume compared to the SMC. This improvement becomes more pronounced at higher rotor speeds and during rapid variations in solar irradiation and temperature, demonstrating the proposed approach's ability to adapt and remain robust under changing environmental conditions.

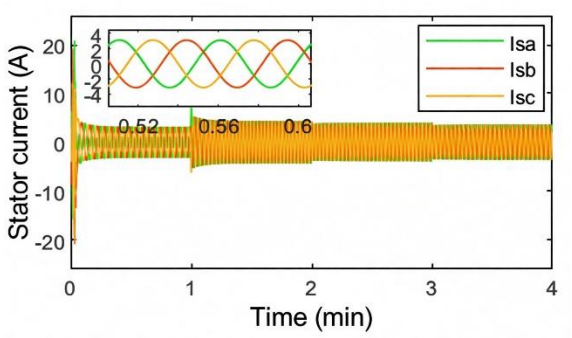

Figures 22. Stator current response under the proposed control approach

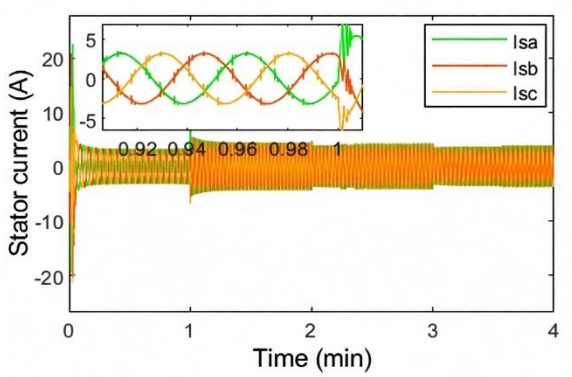

Figures 23. Stator current response under the SMC approach

Table 5. Performance indicators

Irradiation	Proposed control technique		P&O technique/ IM based PID control		SMC technique	
	Oscillation	NSMSE	Oscillation	NSMSE	Oscillation	NSMSE
600	0.13		3.17		0.66	
1000	0.13	10.07	5.75	11.70	1.18	10.29
900	0.17		6.25		0.38	
800	0.15		5.24		1.13	

Finally, Figures 22 and 23 show the stator current waveforms. The proposed control technique produces nearly sinusoidal current profiles, whereas the SMC approach results in visibly distorted waveforms. This improvement demonstrates the effectiveness of the proposed DTC-based strategy in enhancing current quality, reducing harmonic distortion, and consequently improving the overall performance and

energy efficiency of the photovoltaic water pumping system.

The quantitative results reported in Table 5 further validate the proposed control technique superior performance relative to the SMC approach.

5. Conclusion

This work introduces a novel control strategy for photovoltaic water pumping systems (PVWPS), integrating reinforcement learning (RL)-based MPPT and ADRC enhanced by dynamic surface control (DSC) and RL-based induction motor speed regulation. Comprehensive numerical simulations demonstrate that the proposed scheme achieves up to 97.7% and 89% reductions in power oscillations compared to conventional P&O/PID control and sliding mode control (SMC), respectively, alongside improvements in normalized speed mean square error (NSMSE) of up to 13.9% and 2.1%. Additional benefits include reduced torque and flux ripples, smoother stator currents, and increased water pumping efficiency, confirming enhanced tracking accuracy, robustness, and dynamic response. Nevertheless, this study is limited to simulation results, lacking experimental validation. Practical challenges such as partial shading effects, hardware nonlinearities, and fault conditions remain to be investigated. Future efforts will aim to implement the proposed approach on real hardware and validate its performance experimentally, along with enhancing controller adaptability and fault tolerance to enable reliable deployment in off-grid and rural water supply applications.

Acknowledgments

The authors express their gratitude to the anonymous reviewers for their valuable feedback and insightful suggestions.

Nomenclature

a_k	Action selected by the RL agent at step k
α	Duty cycle of the DC–DC boost converter
$\alpha_{\min}, \alpha_{\max}$	Minimum and maximum duty cycle limits
β	Discount factor in the critic cost function
b	Viscous friction coefficient of the induction motor
C_{dc}	DC-link capacitor
d_t	Load torque disturbance
$\hat{d}_t$	Estimated disturbance
ΔV	Reference voltage perturbation step
δ_k	Temporal-difference (TD) error
ϵ	Exploration rate in ε-greedy policy
ε_a^*	Actor approximation error
ε_c^*	Critic approximation error
e_t	Speed tracking error
F	Mechanical friction coefficient
f_s	Switching frequency
γ	Discount factor in RL update
$H(\pi)$	Policy entropy
I_{cc}	Short-circuit current of PV module
I_L	Line current of the induction motor
I_{mpp}	PV current at maximum power point
I_{ph}	Photogenerated current
I_{pv}	Output current of the PV array
I_0	Diode reverse saturation current
$I_{r\alpha}, I_{r\beta}$	Rotor currents in α-β frame
$I_{s\alpha}, I_{s\beta}$	Stator currents in α-β frame
J	Rotor inertia
J_c	Discounted cost function
K_{pump}	Pump torque coefficient
k, k_1, k_2	Control gains
L_{pv}	Boost converter inductance
L_r, L_s	Rotor and stator inductances
M	Mutual inductance
N_p	Number of PV panels connected in parallel
N_s	Number of PV panels connected in series
P	Number of pole pairs
P_k	Instantaneous PV power
P_{mpp}	Maximum power point of PV array
$Q(s,a)$	State–action value function
q	Electron charge
$R(k)$	Instantaneous reward
R_r, R_s	Rotor and stator resistances
R_{sh}	Shunt resistance of PV cell
r_k	Reward signal
S_t	Sliding surface
$\tilde{S}_t$	Sliding surface estimation error
s_k	RL state at step k
T_e	Electromagnetic torque
T_l	Load torque
T_{pump}	Pump load torque
T_s	Sampling period
V_{dc}	DC bus voltage

V_{dc}^{*}	Reference DC bus voltage
V_k	Measured PV voltage
V_{LL}	RMS line voltage of the induction motor
V_{mpp}	PV voltage at maximum power point
V_{oc}	Open-circuit voltage of PV module
V_{out}	Output DC voltage
V_{pv}	PV array voltage
V_{ref}	Reference PV voltage
V_t	Lyapunov function
V_t	Thermal voltage
ϑ	Learning rate
ω	Rotor angular speed
$\widehat{\omega}$	Estimated rotor speed
ω_{ref}	Reference rotor speed
$\widetilde{\omega}$	Speed estimation error
$\phi_{r\alpha}, \phi_{r\beta}$	Rotor flux components
$\phi_{s\alpha}, \phi_{s\beta}$	Stator flux components
ρ_a	Actor learning rate
ρ_c	Critic learning rate
σ_a, σ_c	Actor and critic update bounds
Υ	Lumped bounded uncertainty term
ϑ	Learning rate parameter

References

[1]. Moussi, A., Saadi, A., & Asher, G. M. (2003). Photovoltaic pumping systems technologies trends. LARHYSS Journal, 2, 127-150.

[2]. Daud, A.K. and M.M. Mahmoud. (2005). Solar powered induction motor-driven water pump operating on a desert well: Simulation and field tests. Renewable Energy, 30(5), 701–714. https://doi.org/10.1016/j.renene.2004.02.016

[3]. Ramos, J.S. and H.M. Ramos. (2009). Solar powered pumps to supply water for rural or isolated zones: A case study. Energy for Sustainable Development, 13(3), 151–158. https://doi.org/10.1016/j.esd.2009.06.006

[4]. Hamidat, A., B. Benyoucef, and T. Hartani. (2003). Small-scale irrigation with photovoltaic water pumping system in Sahara regions. Renewable Energy, 28(7), 1081–1096. https://doi.org/10.1016/S0960-1481(02)00058-7

[5]. Liu, Y.H., J.H. Chen, and J.W. Huang. (2014). Global maximum power point tracking algorithm for PV systems operating under partially shaded conditions using the segmentation search method. Solar Energy, 103, 350–363. https://doi.org/10.1016/j.solener.2014.02.031

[6]. Gao, X., et al. (2013). Feasibility evaluation of solar photovoltaic pumping irrigation system based on analysis of dynamic variation of groundwater table. Applied Energy, 105, 182–193. https://doi.org/10.1016/j.apenergy.2012.11.074

[7]. Badoud, E., et al. (2013). Bond graph modeling and optimization of photovoltaic pumping system: Simulation and experimental results. Simulation Modelling Practice and Theory, 36, 84–103. https://doi.org/10.1016/j.simpat.2013.05.001

[8]. Arrouf, M. and S. Ghabrour. (2007). Modelling and simulation of a pumping system fed by photovoltaic generator within the Matlab/Simulink programming environment. Desalination, 209(1-3), 23–30. https://doi.org/10.1016/j.desal.2007.04.004

[9]. Muhsen, D.H., T. Khatib, and F. Nagi. (2017). A review of photovoltaic water pumping system designing methods, control strategies and field performance. Renewable and Sustainable Energy Reviews, 68, 70–86. https://doi.org/10.1016/j.rser.2016.09.129

[10]. López-Luque, R., J. Reca, and J. Martínez. (2015). Optimal design of a standalone direct pumping photovoltaic system for deficit irrigation of olive orchards. Applied Energy, 149, 13–23. https://doi.org/10.1016/j.apenergy.2015.03.107

[11]. Arrouf, M. and N. Bouguechal. (2003). Vector control of an induction motor fed by a photovoltaic generator. Applied Energy, 74(2), 159–167. https://doi.org/10.1016/S0306-2619(02)00142-3

[12]. Kamarzaman, N.A. and C.W. Tan. (2014). A comprehensive review of maximum power point tracking algorithms for photovoltaic systems. Renewable and Sustainable Energy Reviews, 37, 585–598. https://doi.org/10.1016/j.rser.2014.05.045

[13]. Stitou, M., et al. (2019). Output feedback control of sensorless photovoltaic systems, with maximum power point tracking. Control Engineering Practice, 84, 1–12. https://doi.org/10.1016/j.conengprac.2018.10.020

[14]. Stitou, M., et al. (2022). Adaptive output-feedback control design for maximum power point tracking of uncertain photovoltaic systems. IFAC Journal of Systems and Control, 21, 100205. https://doi.org/10.1016/j.ifacsc.2022.100205

[15]. Djeriou, S., A. Kheldoun, and A. Mellit. (2018). Efficiency improvement in induction motor-driven solar water pumping system using golden section search algorithm. Arabian Journal for Science and Engineering, 43(5), 3199–3211. https://doi.org/10.1007/s13369-017-2972-6

[16]. Chen, J., et al. (2025). Irradiance sensorless PSO-based Integral Backstepping and Immersion & invariance algorithm for robust MPPT control with real-climatic microcontroller-in-the-loop

experimental validation. Computers and Electrical Engineering, 123, 110279. https://doi.org/10.1016/j.compeleceng.2025.110279
[17]. Abena Malobe, P., P. Djondine, and P. Ntsama Eloundou. (2023). Meta-heuristic optimization of the neuro-fuzzy MPPT controller for PV systems under partial shading conditions. Journal of Solar Energy Research, 8(1), 1222–1234. https://doi.org/10.22059/jser.2022.349012.1255
[18]. Imani, M. and H. Delavari. (2017). Tuning a PD-type fuzzy controller by particle swarm optimization for photovoltaic systems to achieve maximum power point tracking. Journal of Solar Energy Research, 2(2), 33–39. https://doi.org/10.22059/JSER.2017.62444
[19]. Xiao, Y., et al. (2026). Research on MPPT control strategy based on LSTM and IHOA algorithm. Electric Power Systems Research, 250, 112097. https://doi.org/10.1016/j.epsr.2025.112097
[20]. Ali, K., S. Ullah, and E. Clementini. (2025). Robust Backstepping Super-Twisting MPPT Controller for Photovoltaic Systems Under Dynamic Shading Conditions. Energies, 18(19), 5134. https://doi.org/10.3390/en18195134
[21]. Dunna, V.K., et al. (2024). Super-twisting MPPT control for grid-connected PV/battery system using higher order sliding mode observer. Scientific Reports, 14(1), 16597. https://doi.org/10.1038/s41598-024-67083-w
[22]. Priyadarshi, N., S. Padmanaban, and L. Mihet-Popa. Motor-driven photovoltaic pumping systems using a hybrid ANFIS-FLOWER pollination optimization algorithm. Energies, 11(5), 1067. https://doi.org/10.3390/en11051067
[23]. Akkaya, R., A.A. Kulaksiz, and M. Aydogdu. (2007). DSP implementation of a PV system with GA-MLP-NN based MPPT controller supplying BLDC motor drive. Energy Conversion and Management, 48(1), 210–218. https://doi.org/10.1016/j.enconman.2006.04.022
[24]. Elkholy, M.M. and A. Fathy. (2016). Optimization of a PV fed water pumping system without storage based on teaching-learning-based optimization algorithm and artificial neural network. Solar Energy, 139, 199–212. https://doi.org/10.1016/j.solener.2016.09.022
[25]. El-Khatib, M.F., S. Shaaban, and M.I.A. El-Sebah. (2017). A proposed advanced maximum power point tracking control for a photovoltaic-solar pump system. Solar Energy, 158, 321–331. https://doi.org/10.1016/j.solener.2017.09.051
[26]. Kumar, R. and B. Singh. (2017). Single stage solar PV fed brushless DC motor driven water pump. IEEE Journal of Emerging and Selected Topics in Power Electronics, 5(4), 1377–1385. https://doi.org/10.1109/JESTPE.2017.2699918
[27]. Errouha, M., S. Motahhir, and Q. Combe. (2021). Intelligent control of induction motor for photovoltaic water pumping system. SN Applied Sciences, 3, 777. https://doi.org/10.1007/s42452-021-04757-4
[28]. Ayman, S., et al. (2021). Enhanced quadratic V/f-based induction motor control of solar water pumping system. Energies, 14(15), 4572. https://doi.org/10.3390/en14010104
[29]. Errouha, M., et al., Embedded implementation of improved IFOC for solar photovoltaic water pumping system using dSpace, in Green Energy Technology. 2021, Springer.
[30]. Yahyaoui, I. and A. Serna Cantero, Scalar and vector control of induction motor for online photovoltaic pumping, in Advances in Renewable Energies and Power Technologies. 2018, Elsevier. p. 335–348.
[31]. Krim, S., et al. (2019). Control with high performances-based DTC strategy: FPGA implementation and experimental validation. EPE Journal (European Power Electronics and Drives Journal), 29(2), 82–98. https://doi.org/10.1080/09398368.2018.1548802
[32]. Chergui, M.I. and M. Bourahla. (2013). Application of the DTC control in the photovoltaic pumping system. Energy Conversion and Management, 65, 655–662. https://doi.org/10.1016/j.enconman.2011.08.026
[33]. Gdaim, S., A. Mtibaa, and M.F. Mimouni. (2015). Design and experimental implementation of DTC of an induction machine based on fuzzy logic control on FPGA. IEEE Transactions on Fuzzy Systems, 23(3), 644–655. https://doi.org/10.1109/TFUZZ.2014.2321612
[34]. Tazerart, F., et al. (2015). Direct torque control implementation with losses minimization of induction motor for electric vehicle applications with high operating life of the battery. International Journal of Hydrogen Energy, 40(39), 13788–13798. https://doi.org/10.1016/j.ijhydene.2015.04.052
[35]. Terki, A., et al. (2012). An improved efficiency of fuzzy logic control of PMBLDC for PV pumping system. Applied Mathematical Modelling, 36(3), 934–944. https://doi.org/10.1016/j.apm.2011.07.042
[36]. Chou, K.Y., S.T. Yang, and Y.P. Chen. (2019). Maximum power point tracking of photovoltaic system based on reinforcement learning. Sensors, 19(22), 5054. https://doi.org/10.3390/s19225054
[37]. Zaky, A.A. (2020). Energy efficiency improvement of water pumping system using synchronous reluctance motor fed by perovskite solar cells. International Journal of Energy Research,

44(14), 11629–11642. https://doi.org/10.1002/er.5788
[38]. Loukriz, A., M. Haddadi, and S. Messalti. (2016). Simulation and experimental design of a new advanced variable step size incremental conductance MPPT algorithm for PV systems. ISA Transactions, 62, 30–38. https://doi.org/10.1016/j.isatra.2015.08.006
[39]. Ben Ammar, R., M. Ben Ammar, and A. Oualha. (2020). Photovoltaic power forecast using empirical models and artificial intelligence approaches for water pumping systems. Renewable Energy, 153, 1016–1028. https://doi.org/10.1016/j.renene.2020.02.065
[40]. Prabhakaran, K.K., et al. (2020). Standalone single stage PV fed reduced switch inverter based PMSM for water pumping application. IEEE Transactions on Industrial Applications, 56(6), 6526–6535. https://doi.org/10.1109/TIA.2020.3023870
[41]. Varnham, A., et al. (2007). Soft computing model-based controllers for increased photovoltaic plant efficiencies. IEEE Transactions on Energy Conversion, 22(4), 873–879. https://doi.org/10.1109/TEC.2007.895877
[42]. Hamza, B.K. (2025). Novel active disturbance rejection control law design for nuclear reactor power level control in load following operation. Annals of Nuclear Energy, 218, 111410. https://doi.org/10.1016/j.anucene.2025.111410
[43]. Radke, A. and Z. Gao. A survey of state and disturbance observers for practitioners. in Proceedings of the American Control Conference. 2006.
[44]. Wang, M., et al. (2021). A novel framework for backstepping-based control of discrete-time strict-feedback nonlinear systems with multiplicative noises. IEEE Transactions on Automatic Control, 66(4), 1484–1496. https://doi.org/10.1109/TAC.2020.2995576